Supercritical Dynamics of Baroclinic Disturbances in the Presence of Asymmetric Ekman Dissipation

SHIH-HUNG CHOU AND ARTHUR Z. LOESCH

Department of Atmospheric Science, State University of New York at Albany, Albany, NY 12222

(Manuscript received 24 September 1985, in final form 10 February 1986)

ABSTRACT

Finite-amplitude dynamics of baroclinic waves are examined in the presence of asymmetric Ekman pumping at the lower and upper boundaries. Both asymptotic and spectral numerical methods are employed. The resulting amplitude equations yield time evolutions that can lead to an eventual equilibration, a regular perpetual vacillation or a chaotic vacillation depending on the actual values of the supercriticality, the dissipation and the stratification parameters and the fundamental zonal wavenumber. Within the limits of strong bottom dissipation and weak supercriticality, the system always eventually equilibrates and the asymptotic results compare favorably with the numerical results. The vacillation is most likely to occur when the bottom dissipation is weak, supercriticality is strong or the viscous asymmetry is high. Vacillatory final states are possible for up to an order of magnitude larger bottom dissipation than predicted by the symmetric configuration, provided the top dissipation is small in comparison.

1. Introduction

The majority of the nonlinear studies of baroclinic waves consider the effects produced by the Ekman dissipation to be either negligibly small (the inviscid case) or of the *same* magnitude at both upper and lower boundaries (the symmetric viscous case). The weakly nonlinear analyses of these viscous configurations have been carried out by Pedlosky (1970, 1971, 1972) and Pedlosky and Frenzen (1980) within the context of the two-layer model and by Drazin (1970, 1972) within the context of the Eady (1949) continuous model. In the inviscid case, the wave amplitude enters a perpetual vacillation whose amplitude and period depend on the initial conditions. In the symmetric viscous case the finite-amplitude dynamics exhibit a rich and complex range of behavior which depends on the strength of the Ekman pumping, measured by the dissipation parameter r (defined by 2.2). When $r = O(1)$ the wave amplitude tends monotonically to a steady value; for small r, depending on its actual value, the amplitude can reach a steady state, enter a limit cycle or vacillate chaotically. The solutions are independent of the initial conditions, i.e., the wave gradually loses its "memory" due to the presence of the Ekman pumping.

Recently, the finite-amplitude dynamics of baroclinic waves in a *free-surface* configuration have been studied by Pedlosky (1983) in the framework of the two-layer model, and by Chou and Loesch (1986), hereafter referred to as FS, in the framework of the Eady (1949) model. In both studies, an Ekman layer of strength r is present near the lower boundary while the upper boundary remains stress free. Pedlosky examines asymptotically the *weak* dissipation and *weak* supercriticality limit and restricts the zonal wavenumber to that which lies in the vicinity of the inviscid short-wave cutoff. Chou and Loesch, in the first part of their paper, examine asymptotically the *strong* dissipation, *weak* supercriticality limit, and in the second part explore numerically the *entire* dissipation, supercriticality and wavenumber parameter space. The evolution of the baroclinic wave in this configuration is generally characterized by a growth stage to a maximum amplitude followed by a decay stage. During the decay stage, the spectral numerical solution develops an amplitude vacillation which, for most parameter settings, is relatively weak and chaotic in nature and persists at a mean level of the order of the initial amplitude. The exceptions are (1) moderate and long waves in the strong dissipation limit, for which the vacillation slowly decays, and the system eventually becomes wave free, and (2) short waves in the strong dissipation, weak stratification limit, for which the initial "hump" and the subsequent vacillation are of the same order as the initial amplitude. For sufficiently small viscosity, the system also develops a vacillation during its growth stage. The asymptotic solutions, which always decay to zero, fail to predict the vacillatory final state of the system, but qualitatively capture its growth and early decay.

Each of the foregoing three viscous configurations (inviscid, symmetric viscous and free-surface) yields such a distinct amplitude evolution that it becomes essential to study the nonlinear wave dynamics with *unequal* Ekman dissipation at upper and lower boundaries. The introduction of unequal Ekman pumping

© 1986 American Meteorological Society

Unauthenticated | Downloaded 01/28/22 11:40 PM UTC

at the horizontal boundaries is also physically important in the study of geophysical systems. For example, the troposphere can be envisaged as a layer of fluid confined between the earth's surface and the tropopause and the Ekman pumping associated with the latter is weaker than that near the surface. A similar asymmetry in Ekman pumping is also evident in an oceanic system and in the annulus experiments in the absence of the upper lid (Pfeffer et al., 1980).

Following a brief introduction of the model and examination of its linear dynamics, we address asymptotically, in section 3, the weakly nonlinear problem for strong bottom dissipation while the top dissipation is chosen to be either of the same order of magnitude as the bottom dissipation or very small compared to the bottom dissipation. These two limits are important because they bridge the gap with the known results: the former can be reduced to the symmetric case while the latter can be reduced to the free-surface case. In section 4 we examine the results of a multimode spectral numerical model based on the original model equations. These results serve to assess the accuracy of the asymptotic results and to extend the results in dissipation, shear and wavenumber parameter space.

2. The model and linear analysis

The model employed here is that first introduced by Eady (1949) modified by the presence of Ekman pumping at the upper and lower rigid boundaries. The Ekman pumping is allowed to have *different* magnitude at each horizontal boundary so that the model can serve as a generalization of the previously studied baroclinic instability problems, i.e., the inviscid case, the free-surface case and the symmetric viscous case. The formulation and the nondimensionalization of the model follows that of Pedlosky (1979) with asymmetry in Ekman pumping. Briefly, a Boussinesq fluid of depth D lies on a horizontal plane rotating with a constant angular velocity $(f/2)\vec{k}$ and is confined between two zonally oriented walls a distance L apart. The Rossby number is considered to be small enough so that the dynamics are quasi-geostrophic. The Brunt–Väisälä frequency N_S, in the absence of motion, is assumed to be a constant. Scales U, L, D and L/D are used to nondimensionalize the horizontal velocity, horizontal lengths, vertical distance and time, respectively. The basic flow upon which a perturbation is superimposed is a time independent zonal flow characterized by a constant vertical shear λ. The nondimensional governing equation and the corresponding boundary conditions for the perturbation streamfunction ϕ, scaled by UL, are

$$\nabla^2\phi + \frac{1}{S}\phi_{zz} = 0 \tag{2.1a}$$

$$\phi_x = \frac{\partial^2}{\partial y \partial t_0}\bar{\phi} = 0 \quad \text{at} \quad y = 0, 1 \tag{2.1b}$$

$$\left(\frac{\partial}{\partial t_0} + \lambda z\frac{\partial}{\partial x}\right)\phi_z - \lambda\phi_x + rS\nabla^2\phi + \epsilon J(\phi, \phi_z) = 0 \quad \text{at} \quad z = -\frac{1}{2} \tag{2.1c}$$

$$\left(\frac{\partial}{\partial t_0} + \lambda z\frac{\partial}{\partial x}\right)\phi_z - \lambda\phi_x - r_1 S\nabla^2\phi + \epsilon J(\phi, \phi_z) = 0 \quad \text{at} \quad z = \frac{1}{2}, \tag{2.1d}$$

where ϵ is a measure of the amplitude of the perturbation field, the overbar represents a zonal average and the Jacobian terms, given by $J(g, h) = g_x h_y - h_x g_y$, represent the nonlinear advections in the system. Several parameters appear in (2.1); these are the stratification parameter

$$S = \frac{N_s^2 D^2}{f^2 L^2} \tag{2.2a}$$

and the Ekman dissipation parameters

$$r = \frac{E^{1/2}}{2\text{Ro}} \tag{2.2b}$$

$$r_1 = \frac{E_1^{1/2}}{2\text{Ro}} \tag{2.2c}$$

for the lower and upper boundaries. In (2.2), Ro is the Rossby number and E and E_1 are the Ekman numbers associated with the lower and upper boundary layers, respectively.

Before proceeding to the nonlinear formulation, it is instructive to examine the stability of the basic state to an infinitesimal perturbation. Upon neglecting the terms of $O(\epsilon)$, the solution of the linearized formulation of (2.1) is

$$\phi = A(\cosh 2\mu z + \Lambda \sinh 2\mu z)e^{ik(x-ct_0)}\sin m\pi y + \text{c.c.} \tag{2.3}$$

where m is an integer, k is the zonal wavenumber, A is the wave amplitude,

$$\mu = \frac{S^{1/2}}{2}(k^2 + m^2\pi^2)^{1/2} \tag{2.4}$$

is the inverse of the vertical e-folding distance,

$$c = -i(r + r_1)\frac{\mu}{2kT}(1 + T^2) \pm i\frac{1}{2} \times \left\{(r + r_1)^2\frac{\mu^2}{k^2T^2}(1 + T^2)^2 + \frac{1}{\mu^2 T} \times \left[\lambda^2(1 - \mu T)(\mu - T) - \frac{16rr_1\mu^4 T}{k^2}\right] - i(r - r_1)\frac{2\lambda}{kT}[\mu(1 + T^2) - 2T]\right\}^{1/2} \tag{2.5}$$

Unauthenticated | Downloaded 01/28/22 11:40 PM UTC

is the (complex) phase speed,

$$\Lambda = \frac{2(r - r_1)\mu^2 + i\lambda k(1 - \mu T)}{2(r + r_1)\mu^2 T - 2ik\mu c} \tag{2.6}$$

is a measure of the vertical structure of the wave, $T = \tanh\mu$, and c.c. denotes the complex conjugate. It follows from (2.5) that for the instability to be realized, the vertical shear of the basic flow must exceed the critical value

$$\lambda_c = \frac{4\mu^2}{k} \times \left[\frac{rr_1 T}{(1 - \mu T)(\mu - T) + \left(\frac{r - r_1}{r + r_1}\right)^2 T\left(\mu - \frac{2T}{1 + T^2}\right)^2}\right]^{1/2} \tag{2.7}$$

and the instability is confined in μ space to $0 < \mu < \mu_c$, where μ_c satisfies

$$(1 - \mu_c T_c)(\mu_c - T_c) + \left(\frac{r - r_1}{r + r_1}\right)^2 T_c\left(\mu_c - \frac{2T_c}{1 + T_c^2}\right) = 0. \tag{2.8}$$

It is important to note that the critical shear is $\lambda_c = 0$ for the inviscid case ($r = r_1 = 0$) and the free-surface case ($r \neq 0$, $r_1 = 0$). However, in the free-surface case all shears are unstable irrespective of the vertical e-folding distance μ^{-1} (or, the zonal wavenumber k) while in the inviscid case the instability occurs only when $0 < \mu < \mu_E = 1.1997$, where μ_E represents the inviscid short-wave instability cutoff. The wavenumber corresponding to this cutoff depends on S and m and, from (2.4), is given by

$$k_E = \left(\frac{4\mu_E^2}{S} - m^2\pi^2\right)^{1/2}. \tag{2.9}$$

If neither r or r_1 is negligibly small, instability is possible only when the vertical shear exceeds a *finite* critical value defined by (2.7) and is confined to the region $0 < \mu < \mu_c$, where μ_c is determined from (2.8). When $r = r_1 \neq 0$, $\mu_c = \mu_E$, but when $r_1 < r$, $\mu_c > \mu_E$ and, therefore, the region of instability in the wavenumber space broadens as r_1 is decreased with respect to r. In the limit $r_1 \to 0$, $\mu_c \to \infty$, demonstrating the (linearly) *stabilizing* effect of the upper Ekman dissipation on the short waves. Figure 1 provides several examples of the neutral stability curves ($kc_i = 0$) in the (k, λ) plane of (a) the asymmetric and (b) the symmetric Ekman layer configurations.

3. Asymptotic analysis

The asymptotic development is based on the assumptions that the Ekman dissipation at the lower boundary, r, is O(1) and the actual shear λ exceeds the critical shear λ_c by a small amount compared to r, i.e.,

$$\lambda = \lambda_c + \Delta, \quad \Delta \ll r.$$

Two upper Ekman dissipation limits are considered: $r_1 = O(1)$ and $r_1 = O(|\Delta|^2)$. The former reduces to the symmetric viscous configuration when $r = r_1$, while the latter reduces to the free-surface configuration when $r_1 \to 0$.

a. Limit r, $r_1 = O(1)$

It follows from (2.7) that, when both r and r_1 are O(1), the critical shear λ_c is also O(1). The phase speed and the linear growth rate of the unstable wave are

$$c_r = \lambda_c \frac{r - r_1}{r + r_1}\left(\frac{1}{2} - \frac{T}{\mu(1 + T^2)}\right), \tag{3.1a}$$

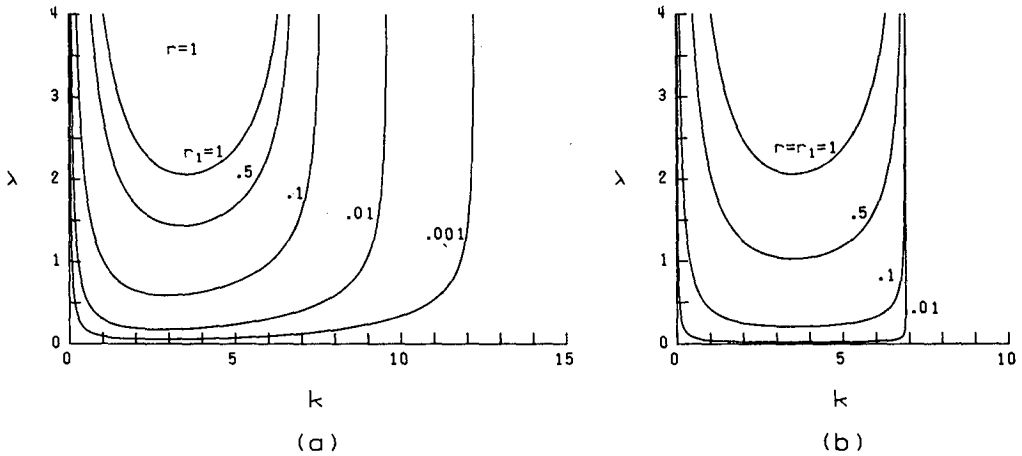

FIG. 1. Marginal stability curves for (a) asymmetric and (b) symmetric viscous configurations for $S = 0.1$.

Unauthenticated | Downloaded 01/28/22 11:40 PM UTC

$$kc_i = \Delta \frac{8\mu^5 T}{\lambda_c} \frac{rr_1(r + r_1)(1 + T^2)}{(r + r_1)^2\mu^4(1 + T^2)^2 + k^2\lambda_c^2\left(\frac{r - r_1}{r + r_1}\right)^2 T^2\left(\mu - \frac{2T}{1 + T^2}\right)^2}. \quad (3.1b)$$

If $r_1 = r$, the unstable wave is stationary and nondispersive, and the steering level is the midlevel of the channel, $z = 0$; if $r_1 < r$, the wave is stationary only when $\mu = \tanh 2\mu \sim 0.96$. For $\mu > 0.96$ the wave propagates westward and the steering level is displaced upward, while for $\mu < 0.96$ the wave propagates eastward and the steering level is displaced downward. Equation (3.1b) suggests that an additional long-time scale given by

$$t = |\Delta| t_0 \quad (3.2)$$

is required to describe the evolution of the unstable wave. By setting $\epsilon = |\Delta|^{1/2}$, (2.1) becomes

$$\left.\begin{aligned}
&\nabla^2\phi + \frac{1}{S}\phi_{zz} = 0 \\
&\phi_x = \frac{\partial^2}{\partial y \partial t}\bar{\phi} = 0 \quad \text{at} \quad y = 0, 1 \\
&\left(\frac{\partial}{\partial t_0} + \lambda_c z \frac{\partial}{\partial x}\right)\phi_z - \lambda_c\phi_x + rS\nabla^2\phi \\
&\quad = -|\Delta|^{1/2} J(\phi, \phi_z) - |\Delta|\left[\left(\frac{\partial}{\partial t} + \frac{\Delta}{|\Delta|} z \frac{\partial}{\partial x}\right) \times \phi_z - \frac{\Delta}{|\Delta|}\phi_x\right] \quad \text{at} \quad z = -\tfrac{1}{2} \\
&\left(\frac{\partial}{\partial t_0} + \lambda_c z \frac{\partial}{\partial x}\right)\phi_z - \lambda_c\phi_x - r_1 S\nabla^2\phi \\
&\quad = -|\Delta|^{1/2} J(\phi, \phi_z) - |\Delta|\left[\left(\frac{\partial}{\partial t} + \frac{\Delta}{|\Delta|} z \frac{\partial}{\partial x}\right) \times \phi_z - \frac{\Delta}{|\Delta|}\phi_x\right] \quad \text{at} \quad z = \tfrac{1}{2}
\end{aligned}\right\}. \quad (3.3)$$

The appropriate asymptotic expansion for the perturbation streamfunction is found to be in the powers of $|\Delta|^{1/2}$, i.e.,

$$\phi = \phi^{(0)} + |\Delta|^{1/2}\phi^{(1)} + |\Delta|\phi^{(2)} + \cdots. \quad (3.4)$$

Substitution of (3.4) into (3.3) yields a sequence of problems for $\phi^{(j)}$. The O(1) problem, arising from the leading terms of (3.3), yields the unstable wave

$$\phi^{(0)} = A(t)(\cosh 2\mu z + \Lambda \sinh 2\mu z)e^{ik(x - ct_0)} \sin m\pi y + \text{c.c.} \quad (3.5)$$

where

$$c = \lambda_c \frac{r - r_1}{r + r_1}\left(\frac{1}{2} - \frac{T}{\mu(1 + T^2)}\right)$$

$$\Lambda = \frac{2(r - r_1)\mu^2 + ik\lambda_c(1 - \mu T)}{2(r + r_1)\mu^2 T - ik\lambda_c \frac{r - r_1}{r + r_1}\left(\mu - \frac{2T}{1 + T^2}\right)}. \quad (3.6)$$

Note that the vertical wave structure Λ is a complex quantity and its imaginary part Λ_i is positive. Therefore, the baroclinic wave has a westward vertical phase shift at marginal instability to maintain itself against dissipation. For consistency, it should be kept in mind that there is an energy source for the basic current even though we do not consider it explicitly.

The $O(|\Delta|^{1/2})$ problem yields the structure of the mean field correction

$$\phi^{(1)} = \Phi(y, z, t) = \sum_{j=1}^{\infty} M_{2j-1}\left(\sinh 2\alpha_{2j-1} z + \frac{r - r_1}{r + r_1} T_{2j-1} \cosh 2\alpha_{2j-1} z\right) \cos(2j - 1)\pi y \quad (3.7)$$

where

$$\left.\begin{aligned}
\alpha_{2j-1} &= S^{1/2}\left(j - \tfrac{1}{2}\right)\pi \\
T_{2j-1} &= \tanh\alpha_{2j-1}
\end{aligned}\right\} \quad (3.8)$$

and the direct relation between the mean field component M_{2j-1} and the wave amplitude A is given by

$$M_{2j-1} = -k\mu \frac{r + r_1}{rr_1} \Lambda_i |A|^2 \frac{\gamma_{2j-1}}{\alpha_{2j-1}^2 \sinh\alpha_{2j-1}} \quad (3.9)$$

where

$$\gamma_{2j-1} = \frac{m^2}{m^2 - \left(j - \frac{1}{2}\right)^2}. \quad (3.10)$$

Finally, the $O(|\Delta|)$ problem yields the equilibration equation for the wave amplitude on the long time scale t,

$$\frac{dA}{dt} = \left(kc_{oi} + i\frac{\Delta}{|\Delta|} G\right)A - N|A|^2 A \quad (3.11)$$

Unauthenticated | Downloaded 01/28/22 11:40 PM UTC

where

$$kc_{oi} = \frac{\Delta}{|\Delta|}\frac{8\mu^5 T}{\lambda_c}\frac{rr_1(r+r_1)(1+T^2)}{(r+r_1)^2\mu^4(1+T^2)^2 + k^2\lambda_c^2\left(\frac{r-r_1}{r+r_1}\right)^2 T^2\left(\mu - \frac{2T}{1+T^2}\right)^2}$$

is the linear growth rate,

$$G = \frac{r-r_1}{r+r_1}\frac{k}{2\mu}\left(\mu - \frac{2T}{1+T^2}\right)\frac{k^2\lambda_c^2 T(1-\mu T)(\mu - T) - (r+r_1)^2\mu^4(1+T^2)^2}{(r+r_1)^2\mu^4(1+T^2)^2 + k^2\lambda_c^2\left(\frac{r-r_1}{r+r_1}\right)^2 T^2\left(\mu - \frac{2T}{1+T^2}\right)^2}$$

is a real quantity,

$$N = \frac{k}{4\mu}\frac{[k\lambda_c(\mu - T) + i(r-r_1)2\mu^2 T]Q_1 + \left[k\lambda_c\frac{r-r_1}{r+r_1}\left(\mu - \frac{2T}{1+T^2}\right) + i(r+r_1)2\mu^2 T\right]Q_2}{(r+r_1)\mu^2(1+T^2) - ik\lambda_c\frac{r-r_1}{r+r_1}T\left(\mu - \frac{2T}{1+T^2}\right)}$$

is the *complex* wave–mean flow interaction coefficient, and

$$Q_1 = \frac{4k\mu\Lambda_i}{rr_1}\sum_{j=1}^{\infty}\frac{\gamma_{2j-1}^2}{\alpha_{2j-1}^2}[(r+r_1)(\alpha_{2j-1}\coth\alpha_{2j-1} - \mu T) + (r-r_1)\Lambda(T\alpha_{2j-1}T_{2j-1} - \mu)],$$

$$Q_2 = \frac{4k\mu\Lambda_i}{rr_1}\sum_{j=1}^{\infty}\frac{\gamma_{2j-1}^2}{\alpha_{2j-1}^2}[(r+r_1)\Lambda(T\alpha_{2j-1}\coth\alpha_{2j-1} - \mu) + (r-r_1)(\alpha_{2j-1}T_{2j-1} - \mu T)]$$

are complex quantities arising from the nonlinear interaction.

Due to the *unequal* dissipation, the wave amplitude A is, in general, a complex quantity and the nonlinear wave–mean flow interaction leads not only to the equilibration of the amplitude modulus but also to the adjustment of the phase speed due to the nonvanishing imaginary part of (3.11). Equation (3.11) is first order in time and it yields a Landau (1944) S-curve amplitude evolution with an equilibrated state given by

$$|A(\infty)| = \left[\frac{kc_{oi}}{N_r}\right]^{1/2} \tag{3.12}$$

while the equilibrated wave propagates at a dispersive speed

$$c - |\Delta|\left[\frac{\Delta}{|\Delta|}G - N_i|A(\infty)|^2\right]\Big/k$$

on the fast-time scale t_0, where N_r and N_i are real and imaginary part of N, respectively.

When $r = r_1$, G and N_i are identically zero. The wave amplitude A becomes purely real. It still undergoes the Landau S-curve equilibration, but, since there is no nonlinear adjustment of the phase speed, the wave becomes nondispersive.

The equilibrated amplitude $|A(\infty)|$ and the corresponding phase speed adjustment $-[G - N_i|A(\infty)|^2]/k$ are given as a function of r_1/r in Fig. 2 for $S = 0.1$, $k = 3.5$ and $r = 1$. Note that the weakly nonlinear theory of this section is not applicable for small r_1/r ratios, since it is based on the assumption that both r and r_1 are O(1). For the parameter combination in Fig. 2, $|A(\infty)|$ decreases with increasing asymmetry; for other parameter combinations the trend can reverse.

b. Limit r = O(1); r_1 = O($|\Delta|^2$)

The mathematical development of this dissipation limit is similar to the free-surface asymptotic development presented in FS. For r = O(1) and r_1 = O($|\Delta|^2$) the critical shear λ_c is an O($|\Delta|$) quantity, while for $r_1 = 0$, $\lambda_c = 0$. When $\lambda = \lambda_c + \Delta$, $\Delta \ll 1$, the phase speed and the linear growth rate are

$$c_r = |\Delta|\hat{\lambda}\left(\frac{1}{2} - \frac{T}{\mu(1+T^2)}\right)$$

and

$$kc_i = |\Delta|^2\left[-\frac{r_1}{|\Delta|^2}\frac{4\mu T}{1+T^2} + \hat{\lambda}^2\frac{k^2}{4r\mu^2}\left(\frac{1-T^2}{1+T^2}\right)^2\left(1 - \frac{T}{\mu(1+T^2)}\right)\right], \tag{3.13}$$

respectively, where

$$\hat{\lambda} = \frac{\lambda_c + \Delta}{|\Delta|}$$

is an O(1) quantity. As in FS, *four* long time variables must be introduced to handle various parts of the disturbance evolution, i.e.,

$$\frac{\partial}{\partial t_0} \to |\Delta|\frac{\partial}{\partial t} + |\Delta|^2\frac{\partial}{\partial \tau_1} + |\Delta|^3\frac{\partial}{\partial \tau_2} + |\Delta|^4\frac{\partial}{\partial \tau_3}. \tag{3.14}$$

Unauthenticated | Downloaded 01/28/22 11:40 PM UTC

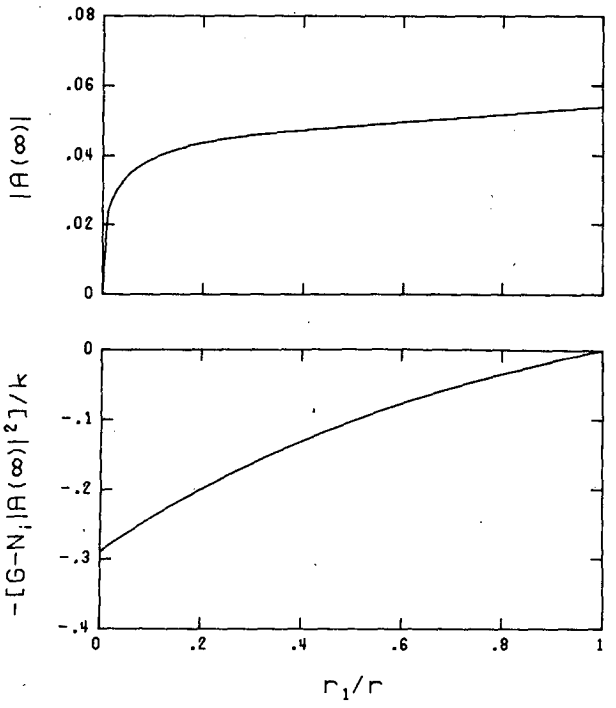

FIG. 2. The equilibrium amplitude, $|A(\infty)|$, and the phase speed correction, $-[G - N_i|A(\infty)|^2]/k$, as functions of the dissipation ratio, r_1/r, for $S = 0.1$, $k = 3.5$ and $r = 1$.

By setting $\epsilon = |\Delta|^2$, the governing equation and the boundary conditions become

$$\left.\begin{aligned}
&\nabla^2\phi + \frac{1}{S}\phi_{zz} = 0 \\
&\phi_x = \frac{\partial^2}{\partial y \partial \tau_n}\bar{\phi} = 0, \quad n = 1, 2, 3, \quad \text{at} \quad y = 0, 1 \\
&rS\nabla^2\phi = -|\Delta|\left[\left(\frac{\partial}{\partial t} + \hat{\lambda}z\frac{\partial}{\partial x}\right)\phi_z - \hat{\lambda}\phi_x\right] \\
&\quad - |\Delta|^2\left[\frac{\partial}{\partial \tau_1}\phi_z + J(\phi, \phi_z)\right] \\
&\quad -|\Delta|^3\frac{\partial}{\partial \tau_2}\phi_z - |\Delta|^4\frac{\partial}{\partial \tau_3}\phi_z \quad \text{at} \quad z = -\frac{1}{2} \\
&\left(\frac{\partial}{\partial t} + \hat{\lambda}z\frac{\partial}{\partial x}\right)\phi_z - \hat{\lambda}\phi_x \\
&\quad = -|\Delta|\left[\frac{\partial}{\partial \tau_1}\phi_z - \frac{r_1}{|\Delta|^2}S\nabla^2\phi + J(\phi, \phi_z)\right] \\
&\quad -|\Delta|^2\frac{\partial}{\partial \tau_2}\phi_z - |\Delta|^3\frac{\partial}{\partial \tau_3}\phi_z \quad \text{at} \quad z = \frac{1}{2}
\end{aligned}\right\}. \tag{3.15}$$

The appropriate expansion for the perturbation streamfunction is

$$\phi = \phi^{(0)} + |\Delta|\phi^{(1)} + |\Delta|^2\phi^{(2)} + \cdots. \tag{3.16}$$

Substitution of (3.16) into (3.15) yields a sequence of problems in powers of $|\Delta|$. The method of analysis is identical to section 3 of FS and the readers should refer to that paper for details. As in FS, four orders in $|\Delta|$ must be considered to close the problem and the final solution consists of a single zonal wave with a *multimode* meridional structure:

$$\begin{aligned}
\tilde{\phi} = A\Bigg\{&\left[\cosh 2\mu z + \left(\frac{1}{T} + i|\Delta|\Lambda^{(1)}\right.\right. \\
&\left.\left. + |\Delta|^2\Lambda^{(2)}\right)\sinh 2\mu z\right]\sin\pi y + |\Delta|^2\sum_{p=1}^{\infty}\Lambda_{2p+1}{}^{(2)} \\
&\times\left(\cosh 2\mu_{2p+1}z + \frac{1}{T_{2p+1}}\sinh 2\mu_{2p+1}z\right) \\
&\times\sin(2p+1)\pi y\Bigg\}e^{ik(x-ct)} + \text{c.c.} + O(|\Delta|^3)
\end{aligned} \tag{3.17}$$

where

$$\Lambda^{(1)} = \frac{k\hat{\lambda}}{2r\mu}\frac{1 - T^2}{T^2}\left(1 - \frac{T}{\mu(1 + T^2)}\right),$$

$$\begin{aligned}
\Lambda^{(2)} = -\frac{k}{4r\mu^2 T}\Bigg\{&\hat{\lambda}\left[2\mu\left(1 - \frac{T}{\mu(1 + T^2)}\right) - T\right] \\
&\times\Lambda^{(1)} + 2\mu c_{oi}\frac{1 - T^2}{T}\Bigg\},
\end{aligned}$$

$$\begin{aligned}
\Lambda_{2p+1}{}^{(2)} = 4\hat{\lambda}^{-1}&\left[1 - \frac{T}{\mu(1 + T^2)}\frac{\mu_{2p+1}(1 + T_{2p+1}{}^2)}{T_{2p+1}}\right]^{-1} \\
&\times\frac{\cosh\mu}{\cosh\mu_{2p+1}}\sum_{j=1}^{\infty}\left(\frac{\alpha_{2j-1}\cosh 2\alpha_{2j-1}}{\cosh\alpha_{2j-1}}\right. \\
&\left. - \frac{\mu(1 + T^2)}{T}\sinh\alpha_{2j-1}\right)\zeta_{2p+1,2j-1},
\end{aligned}$$

$$\zeta_{2p+1,2j-1} = \frac{(2p+1)\left(j - \frac{1}{2}\right)^2}{\left[(p+1)^2 - \left(j - \frac{1}{2}\right)^2\right]\left[p^2 - \left(j - \frac{1}{2}\right)^2\right]},$$

$$\mu_{2p+1} = \frac{S^{1/2}}{2}[k^2 + (2p+1)^2\pi^2]^{1/2},$$

$$T_{2p+1} = \tanh\mu_{2p+1},$$

$$c = \hat{\lambda}\left(\frac{1}{2} - \frac{T}{\mu(1 + T^2)}\right),$$

Unauthenticated | Downloaded 01/28/22 11:40 PM UTC

$$kc_{oi} = \frac{k^2}{4r\mu^2}\left(\frac{1-T^2}{1+T^2}\right)^2 \times \left(1 - \frac{T}{\mu(1+T^2)}\right)\left(1 + 2\frac{\Delta}{|\Delta|}\frac{\lambda_c}{|\Delta|}\right).$$

As in the free-surface configuration [FS, Eq. (3.30)], the wave field (3.17) has a rich meridional structure, generated by the nonlinear interaction of the O(1) wave field and the O($|\Delta|$) mean field correction. The amplitudes of the higher meridional harmonics, which are of O($|\Delta|^2$), depend diagnostically on the fundamental amplitude, i.e., $A_{2p+1} = |\Delta|^2 \Lambda_{2p+1}{}^{(2)} A$. This is in contrast to the r, $r_1 = \mathrm{O}(1)$ limit in which a *single* meridional mode is sufficient to describe the wave field (3.5). The mean field correction is given by

$$\bar{\phi} = |\Delta| \sum_{j=1}^{\infty} M_{2j-1}(\sinh 2\alpha_{2j-1} z + T_{2j-1}\cosh 2\alpha_{2j-1} z) \times \cos(2j-1)\pi y + \mathrm{O}(|\Delta|^2) \quad (3.18)$$

where α_{2j-1} and T_{2j-1} are defined in (3.8). The *reconstituted* equation for the *modulus* of the wave amplitude is

$$\frac{d|A|}{d\tau} = kc_{oi}|A| + |\Delta|^2|A|\left[a_1 + a_2 R + 2k\frac{T}{\mu(1+T^2)}\Lambda^{(1)}\sum_{j=1}^{\infty} M_{2j-1}\gamma_{2j-1} \times \left(T_{2j-1}\frac{\alpha_{2j-1}\cosh 2\alpha_{2j-1}}{\cosh\alpha_{2j-1}} - 2\mu\sinh 2\alpha_{2j-1}\right)\right] \quad (3.19)$$

and the equation for the $(2j-1)$th mean field component is

$$\frac{dM_{2j-1}}{d\tau} = -\frac{r_1}{|\Delta|^2}2\alpha_{2j-1}T_{2j-1}M_{2j-1} + |A|^2\frac{\cosh\alpha_{2j-1}}{\alpha_{2j-1}\cosh 2\alpha_{2j-1}}\left\{-4k\mu\Lambda^{(1)}\gamma_{2j-1} - |\Delta|^2\left[\frac{4k^2\mu}{r}c_{oi}\Lambda^{(1)}T_{2j-1}\gamma_{2j-1}\left(1 - \frac{1}{\cosh 2\alpha_{2j-1}}\right) + 4k\mu\Lambda^{(3)}\gamma_{2j-1} - \frac{2}{\pi}\sum_{p=1}^{\infty}\chi_{2p+1}\zeta_{2p+1,2j-1}\right]\right\} \quad (3.20)$$

where

$$a_1 = -kc_{oi}\frac{T}{1+T^2}\Lambda^{(2)} - \frac{k^2\hat{\lambda}}{4r\mu^2}c_{oi}\frac{T(1-T^2)}{(1+T^2)^2}\Lambda^{(1)} + \frac{k^2\hat{\lambda}^2}{8r\mu^3}\frac{T(1-T^2)}{(1+T^2)^2}\left[2\mu\left(1 - \frac{T}{\mu(1+T^2)}\right) - T\right]\Lambda^{(2)} - \frac{r_1}{|\Delta|^2}2\mu\frac{T^2}{1+T^2}\Lambda^{(2)},$$

$$a_2 = k\frac{T}{1+T^2}\Lambda^{(1)} - \frac{k^2\hat{\lambda}}{4r\mu^2}\left(\frac{1-T^2}{1+T^2}\right)^2,$$

$$R = \frac{k^2\hat{\lambda}^2}{8r\mu^3}\frac{T(1-T^2)}{(1+T^2)^2}\left[2\mu\left(1 - \frac{T}{\mu(1+T^2)}\right) - T\right]\Lambda^{(1)} + \frac{k\hat{\lambda}}{4r\mu^2}c_{oi}\left(\frac{1-T^2}{1+T^2}\right)^2 - \frac{T}{1+T^2}c_{oi}\Lambda^{(1)} - \frac{r_1}{|\Delta|^2}\frac{2\mu}{k}\frac{T^2}{1+T^2}\Lambda^{(1)} + 4\sum_{j=1}^{\infty}M_{2j-1}\gamma_{2j-1}\left(\frac{T}{\mu(1+T^2)}\frac{\alpha_{2j-1}\cosh 2\alpha_{2j-1}}{\cosh\alpha_{2j-1}} - \sinh\alpha_{2j-1}\right),$$

$$\chi_{2p+1} = 2k\pi\cosh\mu\cosh\mu_{2p+1}\left\{\left[2\mu - T\frac{\mu_{2p+1}(1+T_{2p+1}{}^2)}{T_{2p+1}}\right]\Lambda^{(1)}\Lambda_{2p+1}{}^{(2)} + 2\left[\frac{\mu_{2p+1}(1+T_{2p+1}{}^2)}{T_{2p+1}} - \frac{\mu(1+T^2)}{T}\right]\xi_{2p+1} + \left[2\mu_{2p+1} - \frac{\mu(1+T^2)}{T}T_{2p+1}\right]\Lambda_{2p+1}{}^{(3)}\right\},$$

$$\xi_{2p+1} = \frac{1}{2}\hat{\lambda}^{-1}\left[1 - \frac{T}{\mu(1+T^2)}\frac{\mu_{2p+1}(1+T_{2p+1}{}^2)}{T_{2p+1}}\right]^{-1} \times \left[\hat{\lambda}\left(\frac{T}{\mu(1+T^2)}2\mu_{2p+1} - T_{2p+1}\right)\Lambda_{2p+1}{}^{(3)} - 2c_{oi}\frac{\mu_{2p+1}(1+T_{2p+1}{}^2)}{T_{2p+1}}\Lambda_{2p+1}{}^{(2)}\right.$$

Unauthenticated | Downloaded 01/28/22 11:40 PM UTC

$$+ 4\Lambda^{(1)} \frac{\cosh\mu}{\cosh\mu_{2p+1}} \sum_{j=1}^{\infty} M_{2j-1}\left(T \frac{\alpha_{2j-1} \cosh 2\alpha_{2j-1}}{\cosh\alpha_{2j-1}} - 2\mu \sinh\alpha_{2j-1}\right)\zeta_{2p+1,2j-1}\Bigg],$$

$$\Lambda_{2p+1}^{(3)} = \frac{k\hat{\lambda}}{2r}\left(1 - \frac{T}{\mu(1+T^2)}\right)\frac{1 - T_{2p+1}{}^2}{\mu_{2p+1}T_{2p+1}}\Lambda_{2p+1}^{(2)},$$

and

$$\frac{d}{d\tau} = \frac{d}{d\tau_1} + |\Delta|\frac{d}{d\tau_2} + |\Delta|^2\frac{d}{d\tau_3},$$

is the reconstituted long time derivative.

When compared to the free-surface configuration [FS, Eqs. (3.27) and (3.28)], the upper dissipation in the asymmetric viscous configuration contributes in a twofold manner to the amplitude evolution. In the mean field, it reduces the mean field correction so that the flow becomes less stable. In the wave field, it increases the linear growth rate so that the wave reaches a larger maximum amplitude.

Figures 3–5 illustrate the results of numerical integration of (3.19) and (3.20) using a fourth-order Runge-Kutta scheme. The upper limit of the infinite series in (3.17) and (3.18) were truncated at $j = 6$ and $p = 5$. Thus, the highest retained harmonics in y is $11\pi y$. (Recall that only *odd* meridional harmonics are generated by the nonlinear interaction.) This proved to be the *lowest* meridional truncation beyond which no significant change was detected in the solutions. The time interval chosen for numerical integration is $\Delta\tau = 0.01$. Three ratios of $r_1/|\Delta|^2$ were chosen: 10, 1 and 0.04, while all remaining parameters were fixed at $S = 0.1$, $\Delta = 0.1$, $r = 1$ and $k = 3.5$. For the large ratio, $r_1/|\Delta|^2 = 10$, as shown in Fig. 3, the real wave amplitude $|A|$ reaches its equilibrium rapidly. There is a slight "overshot" of wave amplitude which decreases for larger $r_1/|\Delta|^2$ ratios, yielding a more monotonic amplitude evolution which more closely approaches the Landau (1944) S-curve equilibration found in section 3a. For the moderate ratio, $r_1/|\Delta|^2 = 1$, as shown in Fig. 4, $|A|$ equilibrates to a steady state through a damped vacillation. For the small ratio, $r_1/|\Delta|^2 = 0.04$, as shown in Fig. 5a, the wave reaches a maximum amplitude, then decays to a near-zero amplitude state where it persists for a substantial amount of time. This part of the wave revolution is similar to the life cycle of the free-surface configuration, $r_1/|\Delta|^2 = 0$, as shown in Fig. 3a of FS. However, in the presence of the top dissipation the wave is eventually subjected to a second growth followed by a damped vacillation terminating in a nonzero steady state. The difference between the "near free-surface" and the "free-surface" behavior can be further revealed by comparing the time evolution of the first and dominant mean field component M_1 shown in Fig. 5b for $r_1/|\Delta|^2 = 0.04$ and in Fig. 3b of FS for $r_1/|\Delta|^2 = 0$. In the free-surface case, M_1 tends monotonically to a steady value which yields a stable nonlinearly corrected mean shear. In the presence of a small but nonzero top dissipation, after reaching its maximum, M_1 gradually decreases in strength as is required by the $r_1/|\Delta|^2$ term in (3.20). As a result, the vertical shear slowly increases and eventually becomes unstable again. The wave then grows abruptly and enters a damped vacillation whose final steady value depends on both r and r_1. The rate of the mean field buildup is proportional to the top dissipation. Therefore, *the*

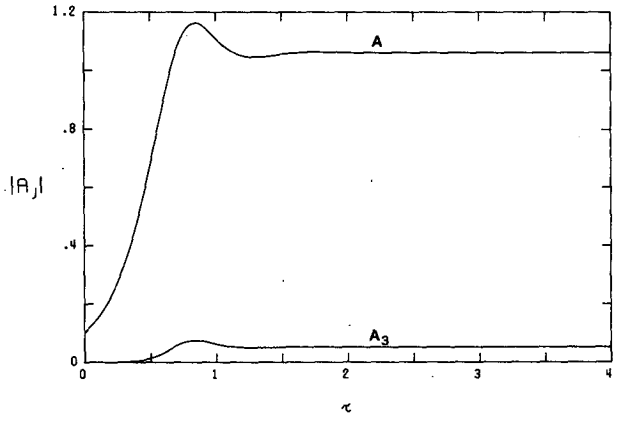

FIG. 3. The time evolution of the real fundamental wave amplitude $|A|$ and the real amplitude of the next nonzero meridional harmonic $|A_3| = |\Delta|^2\Lambda_3^{(2)}|A|$ for the asymptotic system. Parameters are $S = 0.1$, $\Delta = 0.1$, $r = 1$, $r_1/|\Delta|^2 = 10$ and $k = 3.5$.

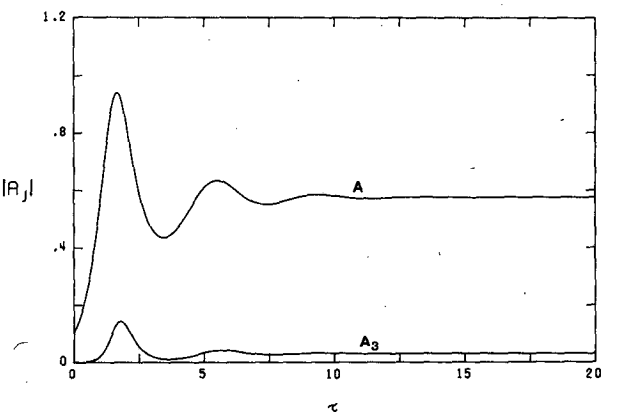

FIG. 4. As in Fig. 3 except $r_1/|\Delta|^2 = 1$.

Unauthenticated | Downloaded 01/28/22 11:40 PM UTC

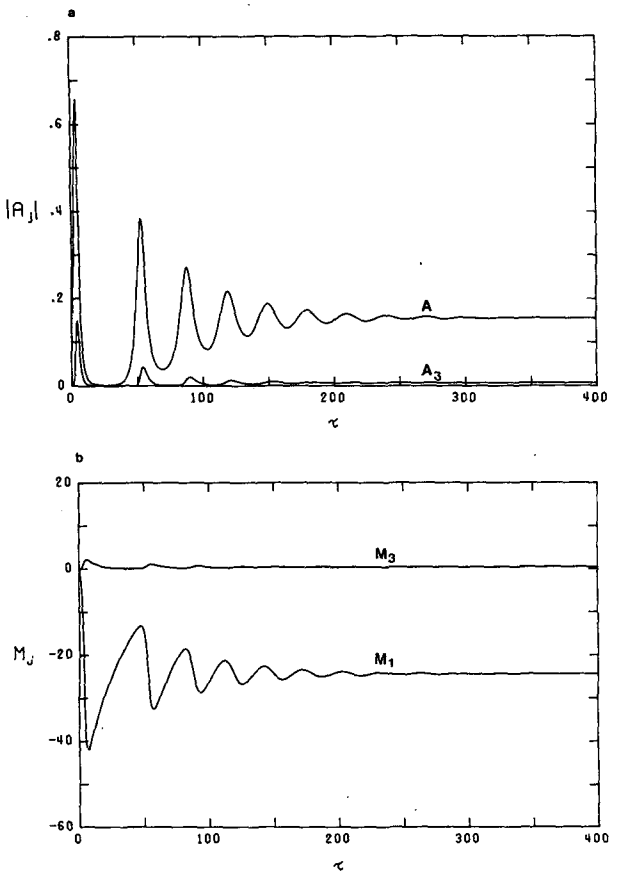

FIG. 5. The time evolution of (a) the real wave amplitudes $|A|$ and $|A_3|$ and (b) the mean field components M_1 and M_3 of the asymptotic system. Parameters are $S = 0.1$, $\Delta = 0.1$, $r = 1$, $r_1/|\Delta|^2 = 0.04$ and $k = 3.5$.

single hump behavior of the free-surface configuration can be envisaged as a limiting behavior of a vacillation with the second hump displaced to infinity.

As is clearly evident from Fig. 5, when $0 < r_1/r \ll 1$, the system evolves through three distinct evolutionary stages: the early stage which closely resembles the free-surface evolution and the duration of which is primarily determined by the bottom dissipation; the intermediate stage characterized by the buildup of the shear and its eventual destabilization and the duration of which is inversely dependent on the top dissipation; and the final stage in which a damped vacillation is found whose equilibrated amplitude depends on the choice of both the top and bottom dissipation. Further numerical experiments (not shown) reveal that as the top dissipation is increased the three stages become less distinct and the wave equilibrates to a larger amplitude in a shorter time. Also, for a fixed top dissipation, an increase in the bottom dissipation results in a larger equilibrated amplitude but requires about the same amount of time to reach it.

4. Spectral numerical model

a. Development

To assess the validity of the asymptotic results obtained in section 3 and, more importantly, to extend the study of the nonlinear dynamics of the asymmetric viscous configuration beyond the asymptotic limits, we develop next a set of spectral equations based on the original set (2.1). In (2.1) we let $\lambda = \lambda_c + \Delta$ and $\epsilon = |\Delta|^2$ and make the substitutions

$$\left.\begin{aligned} t &= |\Delta| t_0 \\ \psi &= |\Delta| \phi \end{aligned}\right\} \tag{4.1}$$

where Δ, the supercriticality, is *not* necessarily small. The wave part of the perturbation streamfunction, $\tilde{\psi}$, is represented by a double Fourier series in x and y:

$$\tilde{\psi} = \sum_{m=1}^{\infty} \sum_{n=1}^{\infty} C_{mn}(z, t) e^{imkx} \sin n\pi y + \text{c.c.} \tag{4.2a}$$

while the zonally averaged part of the perturbation streamfunction, $\bar{\psi}$, is represented by a single Fourier series in y:

$$\bar{\psi} = \sum_{l=1}^{\infty} \bar{C}_l(z, t) \cos l\pi y. \tag{4.2b}$$

In (4.2)

$$\left.\begin{aligned} C_{mn} &= A_{mn}(t) \cosh 2\mu_{mn} z + B_{mn}(t) \sinh 2\mu_{mn} z \\ \bar{C}_l &= M_l(t) \sinh 2\alpha_l z + N_l(t) \cosh 2\alpha_l z \end{aligned}\right\} \tag{4.3}$$

have a vertical structure which satisfies (2.1a), where

$$\mu_{mn} = \frac{S^{1/2}}{2} (m^2k^2 + n^2\pi^2)^{1/2},$$

$$\alpha_l = \frac{S^{1/2}}{2} l\pi.$$

Substituting (4.1) and (4.2) into (2.1c, d) and collecting terms corresponding to a given zonal and meridional harmonic yields a set of spectral evolution equations for C_{mn}'s and $\bar{C}_l$'s at the upper and lower boundaries

$$\frac{\partial}{\partial t}\frac{\partial C_{mn}}{\partial z} = -i\hat{\lambda}mkz\frac{\partial C_{mn}}{\partial z} + i\hat{\lambda}mkC_{mn} + \begin{Bmatrix} -r_1/|\Delta| \\ r/|\Delta| \end{Bmatrix} 4\mu_{mn}{}^2 C_{mn} - \frac{i}{2} k\pi \sum_j \sum_l \sum_p \sum_q \left\{ C_{jl} \frac{\partial C_{pq}}{\partial z} \delta(m, j+p) \right.$$

$$\left. \times [(jq - lp)\delta(n, l+q) + (jq + lp)\,\mathrm{sgn}(l-q)\delta(n, |l-q|)] + \left[C_{jl} \frac{\partial C^*_{pq}}{\partial z} \delta(m, j-p) + C^*_{jl} \frac{\partial C_{pq}}{\partial z} \delta(m, p-j) \right] \right.$$

Unauthenticated | Downloaded 01/28/22 11:40 PM UTC

$$\times [(jq + lp)\delta(n, l + q) + (jq - lp)\,\mathrm{sgn}(l - q)\delta(n, |l - q|)]\Big\} + imk \sum_l \sum_q \left[qC_{ml} \frac{\partial \bar{C}_q}{\partial z} - l\bar{C}_l \frac{\partial C_{mq}}{\partial z} \right]$$

$$\times \left\{ \frac{n}{n^2 - (l - q)^2} [1 - (-1)^{n-l+q}] - \frac{n}{n^2 - (l + q)^2} [1 - (-1)^{n-l-q}] \right\} \quad \text{at} \quad z = \begin{Bmatrix} 1/2 \\ -1/2 \end{Bmatrix},$$

$$\frac{\partial}{\partial t} \frac{\partial \bar{C}_l}{\partial z} = \begin{Bmatrix} -r_1/|\Delta| \\ r/|\Delta| \end{Bmatrix} 4\alpha_l^2 \bar{C}_l - ik \sum_m \sum_n \sum_q m \left(C_{mn} \frac{\partial C^*_{mq}}{\partial z} - C^*_{mn} \frac{\partial C_{mq}}{\partial z} \right)$$

$$\times \left\{ \frac{(n + q)^2}{(n + q)^2 - l^2} [1 - (-1)^{n+q-l}] - \frac{(n - q)^2}{(n - q)^2 - l^2} [1 - (-1)^{n-q-l}] \right\} \quad \text{at} \quad z = \begin{Bmatrix} 1/2 \\ -1/2 \end{Bmatrix}, \quad (4.4)$$

where $\hat{\lambda} = (\lambda_c + \Delta)/|\Delta|$, C^*_{mn} is the complex conjugate of C_{mn} and δ is the Kronecker delta. Note that the transformation (4.1) renders the dependence of the spectral system (4.4) only on the ratio $r/|\Delta|$ rather than r and Δ separately.

The system (4.4) was solved by truncating the infinite series in (4.2) at $m = M$, $n = N$ and $l = L$. The resulting set of $2(M \times N + L)$ coupled first-order equations was then integrated numerically in time using a fourth-order Runge-Kutta scheme. After $\partial C_{mn}/\partial z$ and $\partial \bar{C}_l/\partial z$ were determined at the upper and lower boundaries, the solutions for A_{mn}, B_{mn}, M_l and N_l were obtained using (4.3). Time step $\Delta t = 0.01$ proved to be sufficiently accurate for most integrations. The initial conditions chosen for the majority of the calculations were $A_{11}(0) = 0.01$; $B_{11}(0)$ calculated so that the initial growth rate of A_{11} equals to that predicted by the linear theory; all remaining wave amplitudes in (4.2a) $A_{mn}(0) = B_{mn}(0) = 0$ and all mean field components in (4.2b) $M_l(0) = N_l(0) = 0$, $l \geq 1$. With the chosen initial conditions, $C_{mn} = 0$ for $m + n$ odd and $\bar{C}_l = 0$ for l even.

b. *Importance of truncation*

Before examining the behavior of the spectral system (4.4) in the (S, k, $r/|\Delta|$, r_1/r) parameter space, an extensive test of the truncation was conducted with parameters fixed at $S = 0.1$, $r/|\Delta| = 1$, $r_1/r = 0.1$ and $k = 3.5$. When the wave field is represented by a *single* zonal wave with a *single* meridional mode, i.e., $M = N = 1$, irrespective of the truncation level of L, the solution always reaches a steady state via a damped vacillation. However, for $M \geq 1$ and $N \geq 3$, the solution alters its character to a regular perpetual vacillation. With increasing M or N, this vacillation differs quantitatively in amplitude range and period until $M = 4$ and $N = L = 8$, a truncation beyond which no substantial changes were detected in the solution.

Further tests showed that higher meridional harmonics are more important than zonal harmonics in determining the evolution character of the system for a stronger bottom dissipation (as is also apparent from the asymptotic development in section 3b) or for a larger top to bottom dissipation ratio (in which case the region of instability in the wavenumber-shear domain becomes narrower and, thus, fewer zonal harmonics are unstable). In contrast, as the bottom dissipation becomes weak, or the viscous asymmetry becomes strong, the effects of the higher zonal and meridional harmonics become equally important and more pronounced. For example, when $r/|\Delta|$ is reduced from 1 to 0.1 or r_1/r is reduced from 0.1 to 0.02, the minimum truncation level required for accuracy becomes $M = 6$, $N = L = 12$.

Based on the tests, the single wave system, $M = 1$, $N = L = 12$ can qualitatively capture the evolution character of the solution provided that the choice of $r/|\Delta|$ or r_1/r is made away from the immediate vicinity of the inviscid and the free-surface configurations. For small $r/|\Delta|$ and/or r_1/r, to assure accuracy, the $M = 6$, $N = L = 12$ truncation, which consists of 36 wave components and 6 mean field components, is required to describe the streamfunction (4.2a, b). Due to prohibitive computer cost, in obtaining the results which follow, this truncation was used discriminatingly at selective parameter points either for comparison or to expand the region of validity of the results in parameter space.

c. *Results*

Figure 6 demonstrates, in the viscous parameter space, the striking difference in solution character between the ad hoc single mode truncation, (M, N; L) = (1, 1; 12) and the single wave zonal truncation, (M, N; L) = (1, 12; 12), and the similarity in the solution character between the single wave zonal truncation and the multiwave zonal truncation, (M, N; L) = (6, 12; 12), for $S = 0.1$ and $k = 3.5$. The ordinate is a measure of the bottom dissipation, $r/|\Delta|$, and the abscissa is a measure of the top dissipation as a fraction of the bottom dissipation, r_1/r. Hence, the left vertical axis represents the free-surface configuration, the right vertical axis represents the symmetric viscous configuration and the bottom horizontal axis represents the inviscid configuration.

Unauthenticated | Downloaded 01/28/22 11:40 PM UTC

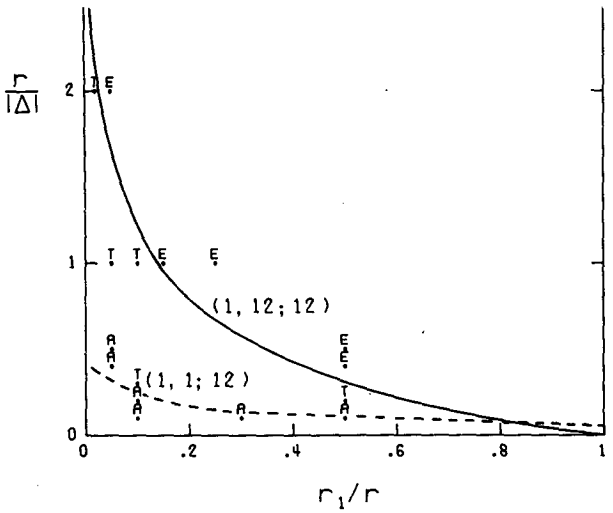

FIG. 6. The boundary curves separating the equilibrated and vacillatory final states for the (1, 12; 12) truncation (solid line) and the (1, 1; 12) truncation (dashed line) when $S = 0.1$ and $k = 3.5$. The solutions of the (6, 12; 12) truncation are marked with E for the equilibrated final state, T for the regular vacillation and A for the chaotic vacillation.

Depending on the amount of dissipation and its asymmetry, two basic types of solutions for each truncation were found: an equilibrating solution and a vacillatory solution. In general, the equilibrating solutions occur for larger values of $r/|\Delta|$ and/or r_1/r than the vacillatory solutions. The curves which separate these two types are drawn as a solid line for the (1, 12; 12) truncation and a dashed line for the (1, 1; 12) truncation. The behavior of the multiwave system, (6, 12; 12), is determined only at select parameter points. They are marked in Fig. 6 by E for equilibrated final state, T for regular perpetual vacillation or A for aperiodic (chaotic) vacillation.

The transition curve separating the equilibrated and vacillatory final states of the single wave (1, 12; 12) system is much steeper than that of the ad hoc (1, 1; 12) system, especially near the free-surface axis where the vacillation can occur for the (1, 12; 12) truncation at a bottom dissipation an order of magnitude larger than for the (1, 1; 12) truncation. In contrast, near the symmetric axis, the (1, 12; 12) solution can vacillate only at a smaller bottom dissipation than the (1, 1; 12) solution. Finally, on the symmetric axis the (1, 12; 12) solution ceases to vacillate except in the immediate vicinity of the inviscid point, $r/|\Delta| = 0$, while the (1, 1; 12) solution still vacillates at $r/|\Delta| = 0.15$. The transition of the single wave (1, 12; 12) system is, however, in close agreement with that of the multiwave (6, 12; 12) system. This is due to the fact that, for the chosen S and k, the transition is sufficiently far from either the free surface or the inviscid axis to make the higher zonal harmonics relatively unimportant in its determination.

To compare the results of the asymptotic system and the multiwave numerical system, we chose the parameter setting: $S = 0.1$, $k = 3.5$, $r = 1$ and $\Delta = 0.1$ (i.e., $r/|\Delta| = 10$). For the dissipation ratio $r_1/r = 0.5$, both the spectral and the asymptotic solutions display a Landau S-curve equilibration whose amplitude is within 1% of each other (after the proper scaling conversions are made). For the ratio $r_1/r = 0.0004$, which approaches the free-surface axis, both solutions display a similar three-stage evolution pattern but the asymptotic solution, shown in Fig. 5, underestimates the final amplitude $|A_{11}(\infty)|$ by 7%.

As the bottom dissipation is decreased, the steady final state, which is always attained in the strong bottom dissipation asymptotic limit, $r/|\Delta| \gg 1$, gradually gives way to a perpetual vacillation. This most readily occurs near the free-surface axis, as is already evident from Fig. 6. We examine the effects of the dissipation ratio, r_1/r, on the amplitude behavior by choosing $S = 0.1$, $k = 3.5$ and $r/|\Delta| = 1$. On the free-surface axis, as shown in FS, the fundamental wave amplitude grows exponentially, reaches a maximum value, then decays to a mean level comparable to the initial amplitude about which it vacillates *chaotically* (Fig. 7). When a very small amount of dissipation is included at the upper boundary, completely different intermediate and final states emerge. The system instead decays to a nearly wave-free state where it persists for a substantial period of time (as is also evident in the asymptotic results shown in Fig. 5), but then grows abruptly and settles into a regular vacillation whose mean level is larger than the initial amplitude. This is illustrated in Fig. 8 for $S = 0.1$, $r/|\Delta| = 1$, $r_1/r = 0.05$ and $k = 3.5$. Note that in the asymmetric configuration the vacillation can occur when the bottom dissipation and the supercriticality are of the same order, provided the top dis-

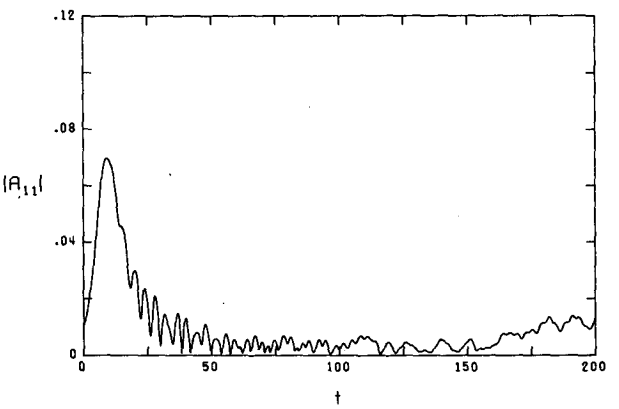

FIG. 7. The time evolution of the real amplitude, $|A_{11}|$ of the spectral numerical system, (6, 12; 12), fopr $S = 0.1$, $r/|\Delta| = 1$, $r/r = 0$ and $k = 3.5$.

Unauthenticated | Downloaded 01/28/22 11:40 PM UTC

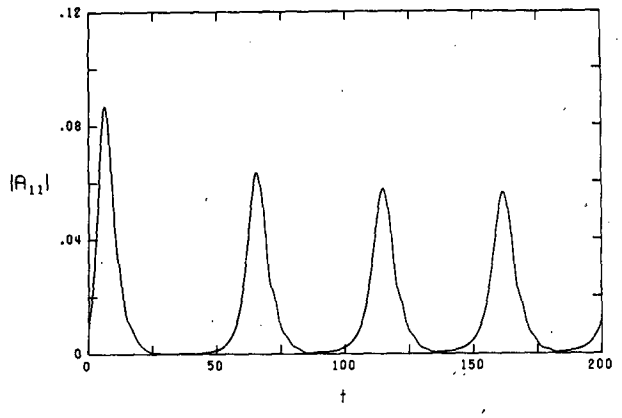

FIG. 8. As in Fig. 7 except $r_1/r = 0.05$.

sipation is small in comparison. A similar three-stage amplitude evolution with a vacillatory final state has been observed in the "free-surface" annulus experiments of Pfeffer (private communication, 1985). Furthermore, both in this study and in the experiments, the vacillation occurs at much larger values of the bottom dissipation than predicted by the symmetric viscous configuration.

The intermediate, nearly wave-free stage of evolution becomes more pronounced and of longer duration as $r/|\Delta|$ and/or r_1/r is decreased. The abrupt growth of the wave amplitude in the asymmetric configuration is due to the mechanism described in the asymptotic treatment (section 3b); i.e., the gradual buildup of the mean field due to the presence of small but nonzero top dissipation.

As r_1/r is increased, while $r/|\Delta|$ remains fixed, the three-stage behavior of Fig. 8 becomes less distinct and the individual amplitude fluctuations in the final stage becomes stronger and more rapid. For the present value of $r/|\Delta| = 1$, the vacillation begins to slowly damp, yielding a steady final state at $r_1/r = 0.15$. As r_1/r is further increased, the damping becomes stronger and finally on the symmetric axis, $r_1/r = 1$, the wave evolution takes on a different character. In the asymmetric interior, the wave amplitude always remains positive while on the symmetric axis it can cross the zero amplitude line, especially for small $r/|\Delta|$. Phase plane diagrams illustrating the change in amplitude evolution from $r_1/r = 0.9$ to $r_1/r = 1$ for $r/|\Delta| = 0.2$ are shown in Fig. 9. In the asymmetric interior, the amplitudes A_{11} and B_{11} are complex, while on the symmetric axis A_{11} is purely real and B_{11} purely imaginary. In the asymmetric case, the real and imaginary parts of the A_{11} (and B_{11}) never reach zero simultaneously but in the symmetric case A_{11} can reach zero and change sign. Due to this phase character, in the asymmetric configuration the wave is propagating and dispersive, while in the symmetric configuration it is nonpropagating and nondispersive. This is also apparent from the asymptotic development in section 3a.

As $r/|\Delta|$ is further reduced, the range of r_1/r over which the vacillation prevails expands toward the symmetric axis. Most of the vacillatory region is occupied by regular vacillations, similar to that shown in Fig. 8. In a multiwave (6, 12; 12) system, chaotic vacillation emerges only in *one* narrow subregion adjoining the inviscid and the free-surface axes marked A in Fig. 6. It occurs at a smaller value of $r/|\Delta|$ for a larger r_1/r. For $S = 0.1$ and $k = 3.5$, the chaotic vacillation appears at $r_1/r = 0.05$ for $r/|\Delta| \leqslant 0.5$, at $r_1/r = 0.1$ for $r/|\Delta| \leqslant 0.2$ and at $r_1/r = 0.5$ for $r/|\Delta| \leqslant 0.1$. An example of the chaotic vacillation is given in Fig. 10 for $r/|\Delta| = 0.1$ and $r_1/r = 0.1$. In contrast, in the ad hoc (1, 1; 12) truncation the chaotic vacillation occurs within *two* subregions of the vacillatory domain: one adjoining the free-surface axis for $0.045 \leqslant r/|\Delta| \leqslant 0.095$ and extending to $r_1/r \sim 0.25$; the second adjoining the symmetric axis for $0.04 \leqslant r/|\Delta| \leqslant 0.07$ and extending to $r_1/r \sim 0.9$. Relatively large areas separating the regular and chaotic vacillations are occupied by higher-period vacillations. That is, in these regions the solution undergoes a hierarchy of bifurcations, characterized by

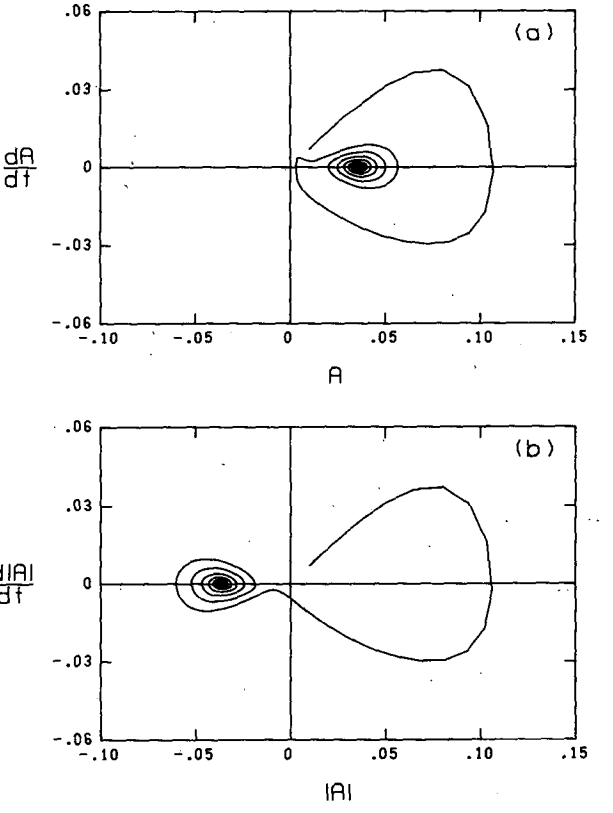

FIG. 9. Phase plane diagrams when (a) $r_1/r = 0.9$ and (b) $r_1/r = 1$ for $S = 0.1$, $r/|\Delta| = 0.2$ and $k = 3.5$.

Unauthenticated | Downloaded 01/28/22 11:40 PM UTC

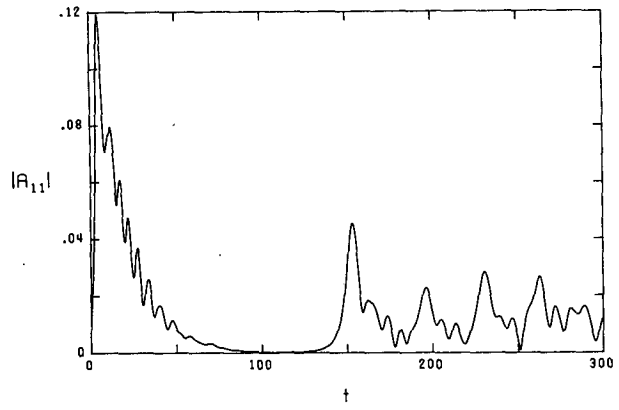

FIG. 10. As in Fig. 7 except $r/|\Delta| = 0.1$ and $r_1/r = 0.1$.

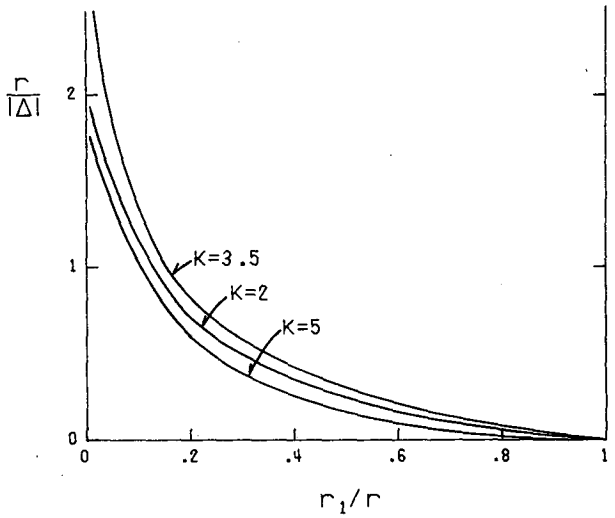

FIG. 11. The boundary curves separating the equilibrated and the vacillatory final state for $k = 2$, 3.5 and 5, while S is fixed at $S = 0.1$.

successive period doubling with higher-period vacillation occupying a narrower dissipation range. These higher-period vacillations, together with the chaotic vacillations, account for about 25% of the whole vacillatory region. In the multiwave (6, 12; 12) system, the chaotic and higher-period vacillations occupy only about 15% of the vacillatory region and the majority of it is occupied by chaotic vacillation. The single wave (1, 12; 12) system does not always reproduce the higher period and chaotic multiwave results due to their proximity to the inviscid and the free-surface axes. For example, in Fig. 6 at $r/|\Delta| = 0.5$ and $r_1/r = 0.05$ the (6, 12; 12) system displays a chaotic vacillation, while the (1, 12; 12) system displays a regular vacillation.

Discussion thus far has concentrated on the time evolution of the system in the viscous parameter space when $S = 0.1$ and $k = 3.5$ which, for this S, corresponds to the most unstable wavenumber of the symmetric viscous configuration. The changes in time evolution with the zonal wavenumber have also been examined using mainly the (1, 12; 12) truncation which, we recall, is quite accurate away from the vicinity of the free surface or the inviscid axis. Figure 11 compares the boundary curves separating the vacillatory and steady final states for $k = 2$, 3.5 and 5 while S is fixed at 0.1. For both longer and shorter waves, $k = 2$ and 5, the boundary curves drop to lower values of $r/|\Delta|$ and the waves are more likely to equilibrate. Further increase in the wavenumber lowers the boundary curves even more and at $k = 6.85$, i.e., in the vicinity of the inviscid Eady cutoff k_E, vacillation exists only very near or on the inviscid axis. In general, for fixed S, $r/|\Delta|$ and r_1/r, a longer wave reaches a *larger* maximum amplitude and either settles into a *stronger* vacillation with a *larger* mean amplitude level or reaches a *larger* equilibrated amplitude. This can be seen by comparing Fig. 12 where $k = 2$ with Fig. 8 where $k = 3.5$.

Finally, we examine the effects of the stratification S on the evolution of waves in the asymmetric configuration, again, using mainly the (1, 12; 12) truncation. Figure 13 depicts the transition curves between the steady and the vacillatory final states for $S = 0.1$ and 0.03 when $k = 3.5$. As the fluid becomes more weakly (strongly) stratified, the region of amplitude vacillation in the $(r_1/r, r/|\Delta|)$ diagram expands (contracts). However, the expansion (contraction) is more pronounced with decreasing r_1/r. As a result, when $S = 0.03$, the vacillation of the system can occur for values of bottom dissipation more than an order of magnitude greater than for the symmetric viscous configuration when the viscous asymmetry is strong. In contrast, when $S = 0.3$, vacillatory final states in Fig. 13 occur only in the immediate vicinity of the inviscid axis.

5. Conclusions and remarks

The supercritical dynamics of the Eady (1949) model are examined in the presence of asymmetric Ekman pumping at the top and bottom boundaries. Both

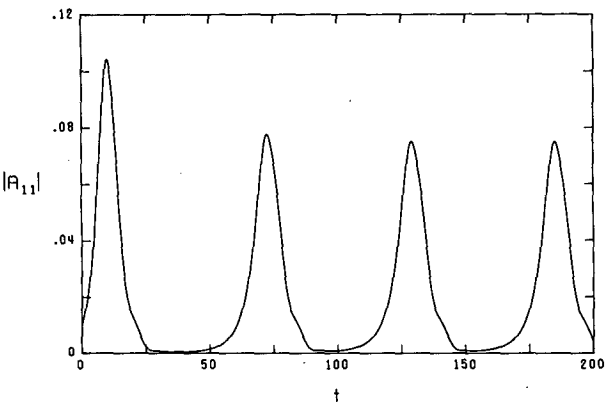

FIG. 12. As in Fig. 7 except $r_1/r = 0.05$ and $k = 2$.

Unauthenticated | Downloaded 01/28/22 11:40 PM UTC

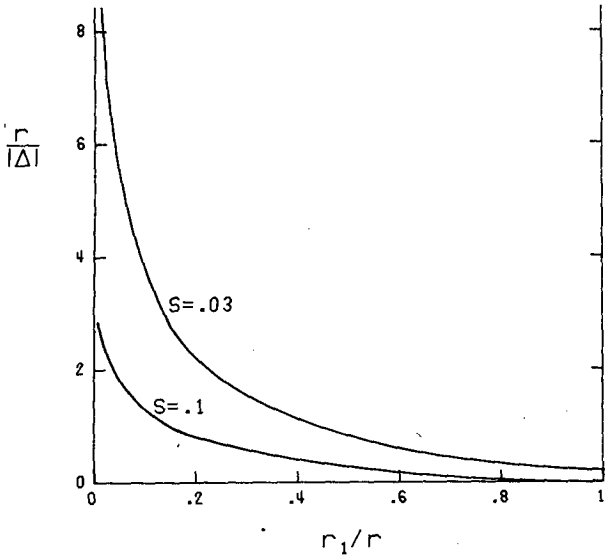

FIG. 13. As in Fig. 11 except for $S = 0.03$ and 0.1 while k is fixed at $k = 3.5$.

asymptotic and numerical methods are employed to study its nonlinear dynamics. The asymptotic methods pivot about the constraints of weak supercriticality and strong bottom dissipation, while the top dissipation is chosen to be either of the same order as the bottom dissipation or very small in comparison. The former case reduces to the symmetric viscous configuration and the latter case reduces to the free-surface configuration, when the corresponding limits are taken.

When the top and bottom dissipations are strong and comparable, the asymptotic wave field is described by a *single* zonal wave and a *single* meridional mode and the solution displays a Landau (1944) S-curve equilibration, similar to that found in the symmetric, strongly viscous configuration. However, unlike in the symmetric configuration, the wave is propagating and dispersive.

When the top dissipation is very small compared to the bottom dissipation, a *single* zonal wave with a *multimode* meridional structure is required to describe the asymptotic wave field. Its solutions range from the Landau S-curve equilibration, to a damped vacillation and, finally, to a three-stage evolution pattern, as the top dissipation is decreased. The three-stage evolution consists of a single-hump early stage similar to the life cycle of the free-surface configuration, a nearly wave-free intermediate stage during which the mean field gradually builds up and leads to an abrupt second growth of the wave, and the final stage in which a damped vacillation is always found.

The spectral numerical method, in which no parameter restriction is required, allows for a rich spectrum of zonal and meridional harmonics and, therefore, captures both wave–mean flow and wave–wave interactions. When the bottom dissipation is *strong*, the higher meridional harmonics become increasingly more important as the top dissipation is reduced, as is also apparent from the asymptotic results. However, as the bottom dissipation is decreased or the supercriticality is increased, the higher meridional harmonics become important for *all* dissipation ratios and, in the highly asymmetric configuration, the zonal harmonics also become crucial in determining the evolution character of the system. Therefore, when the dissipation is weak and/or its asymmetry is high, a truncation consisting of 6 zonal harmonics and 12 meridional harmonics is necessary at higher supercriticality to assure accuracy of the solution. Outside these limits, a single zonal wave with 12 meridional harmonics is sufficiently accurate to capture the evolution character of the system.

The asymptotic solutions compare favorably, in the region of their validity, to the numerical solutions. Away from the asymptotic limits, as the bottom dissipation is reduced and/or the supercriticality is increased, instead of eventually equilibrating, the solution can remain vacillatory. In the viscous parameter space, the vacillatory domain expands toward higher bottom dissipation as the viscous asymmetry increases. As a result, in a highly asymmetric configuration, the vacillation occurs at a much larger bottom dissipation than predicted by the single mode symmetric theories. In contrast, near or at symmetry, vacillations are found only at much lower dissipation than predicted by such theories.

The vacillatory domain is, for the most part, occupied by regular vacillations. Chaotic and higher-period vacillations emerge only when the supercriticality is high, the dissipation is weak and the asymmetry is strong. The curves which separate the vacillatory and equilibrated solutions in the $(r_1/r,\ r/|\Delta|)$ viscous parameter space become steeper and the vacillatory region expands to larger values of the bottom dissipation as the fluid becomes more weakly stratified or as the fundamental wave becomes (linearly) more unstable.

The Eady (1949) model we have examined ignores the β-effect and describes unstable normal modes characterized by zero potential vorticity in the fluid interior. As a result, the mean fields are also characterized by zero potential vorticity. If $\beta \neq 0$ and/or the disturbance potential vorticity is nonzero initially, the fluid interior is described instead by coupled nonlinear potential vorticity equations for the disturbance and the mean flow. Since this system of equations would yield a vertical structure different from (4.3), it is not clear to what extent the results obtained here would remain valid. To simulate the β-effect, without resorting to finite-differencing in the vertical, we have modified the model to include a sloping bottom in the lower boundary condition (2.1c). As expected, based on the linear considerations, a positive northward slope yields

Unauthenticated | Downloaded 01/28/22 11:40 PM UTC

an expanded (contracted) region of equilibrations (vacillations) in Figs. 6, 11 and 13. Further work which examines in detail the effect of bottom topography variations on supercritical baroclinic disturbance is in progress.

Acknowledgments. The work was supported by the National Science Foundation under Grants ATM811740301 and ATM8411327. Acknowledgment is also made to the National Center for Atmospheric Research, which is supported by the National Science Foundation, for computer time used in this research. We are grateful to an anonymous reviewer for his helpful comments and suggestions.

REFERENCES

Chou, S.-H., and A. Z. Loesch, 1986: Supercritical dynamics of baroclinic disturbances in a free-surface model. *J. Atmos. Sci.*, **43**, 285–301.

Drazin, P. G., 1970: Nonlinear baroclinic instability of a continuous zonal flow. *Quart. J. Roy. Meteor. Soc.*, **96**, 667–676.

——, 1972: Nonlinear baroclinic instability of a continuous zonal flow of viscous fluid. *J. Fluid Mech.*, **55**, 577–587.

Eady, E. T., 1949: Long waves and cyclone waves. *Tellus*, **1**, 33–52.

Landau, L. D., 1944: On the problem of turbulence. *C. R. Acad. Sci. USSR.*, **44**, 311–314.

Pedlosky, J., 1970: Finite-amplitude baroclinic waves. *J. Atmos. Sci.*, **27**, 15–30.

——, 1971: Finite-amplitude baroclinic waves with small dissipation. *J. Atmos. Sci.*, **28**, 587–597.

——, 1972: Limit cycles and unstable baroclinic waves. *J. Atmos. Sci.*, **29**, 53–63.

——, 1979: *Geophysical Fluid Dynamics.* Springer-Verlag, 624 pp.

——, 1983: The growth and decay of finite-amplitude baroclinic waves. *J. Atmos. Sci.*, **40**, 1863–1876.

——, and C. Frenzen, 1980: Chaotic and periodic behavior of finite-amplitude baroclinic waves. *J. Atmos. Sci.*, **37**, 1177–1196.

Pfeffer, R. L., G. Buzyna and R. Kung, 1980: Time-dependent modes of behavior of a thermally-driven rotating fluid. *J. Atmos. Sci.*, **37**, 2129–2149.

Unauthenticated | Downloaded 01/28/22 11:40 PM UTC